ACS APPLIED MATERIALS & INTERFACES

www.acsami.org Research Article

Halide Segregated Crystallization of Mixed-Halide Perovskites Revealed by In Situ GIWAXS

Lena Merten,* Timo Eberle, Ekaterina Kneschaurek, Niels Scheffczyk, Paul Zimmermann, Ivan Zaluzhnyy, Azat Khadiev, Florian Bertram, Fabian Paulus, Alexander Hinderhofer, and Frank Schreiber

Cite This: *ACS Appl. Mater. Interfaces* 2024, 16, 8913−8921

Read Online

ACCESS | Metrics & More | Article Recommendations | Supporting Information

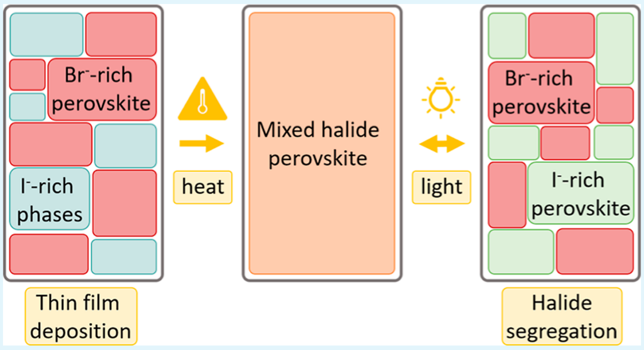

ABSTRACT: Mixed-halide perovskites of the composition $MAPb(Br_xI_{1-x})_3$, which seem to exhibit a random and uniform distribution of halide ions in the absence of light, segregate into bromide- and iodide-rich phases under illumination. This phenomenon of halide segregation has been widely investigated in the photovoltaics context since it is detrimental for the material properties and ultimately the device performance of these otherwise very attractive materials. A full understanding of the mechanisms and driving forces has remained elusive. In this work, a study of the crystallization pathways and the mixing behavior during deposition of $MAPb(Br_xI_{1-x})_3$ thin films with varying halide ratios is presented. In situ grazing incidence wide-angle scattering (GIWAXS) reveals the distinct crystallization behavior of mixed-halide perovskite compositions during two different fabrication routes: nitrogen gas-quenching and the lead acetate route. The perovskite phase formation of mixed-halide thin films hints toward a segregation tendency since separate crystallization pathways are observed for iodide- and bromide-rich phases within the mixed compositions. Crystallization of the bromide perovskite phase ($MAPbBr_3$) is already observed during spin coating, while the iodide-based fraction of the composition forms solvent complexes as an intermediate phase, only converting into the perovskite phase upon thermal annealing. These parallel crystallization pathways result in mixed-halide perovskites forming from initially halide-segregated phases only under the influence of heating.

KEYWORDS: *perovskite, thin films, crystallization, in situ GIWAXS, halide segregation, photovoltaics*

INTRODUCTION

One of the major assets of hybrid metal-halide perovskite materials is their ease of component substitution and mixing. Tunability of material properties, in particular the band gap, is an important result of this, making perovskite materials promising candidates for photovoltaic and related applications.[1,2] In particular, halide mixing, in most cases iodide and bromide, has been widely investigated to adjust bandgaps to desired values, which, for example, are optimized for tandem applications.[3] However, such mixed-halide compositions exhibit a reversible phase separation into iodide- and bromide-rich phases upon injection of charge carriers either directly[4] or via illumination.[5] This is detrimental for applications in several ways, such as the creation of low-bandgap domains,[6,7] thus essentially revoking bandgap tuning. Therefore, an understanding of the driving forces and mechanisms behind halide mixing and segregation is essential.

Several mechanisms have been proposed to explain the phenomenon, including thermodynamic models,[8,9] polaronic strain models,[7,10,11] redox reactions,[12] emergence of internal electric fields due to carrier trapping,[13,14] and various combinations of these.[15] So far, there seems to be no consensus on the exact separation mechanism other than the fact that charge carriers, which can be induced via illumination of the photovoltaically active material, play an integral role.[16] Remixing in the dark is considered to be entropically driven,[16] while different models have predicted different extents of the miscibility gap.[8,9] The question of whether halide segregation is an intrinsic material property or if defects, such as grain boundaries and surfaces, are necessary is not yet clarified.[10,17] A preferred occurrence of halide segregation in defect-rich materials has been found,[17] which might account for defects as promoting factors. On the other hand, a stochastic nucleation of iodide-enriched domains has also been reported,[10] pointing

Received: December 12, 2023
Revised: January 18, 2024
Accepted: January 24, 2024
Published: February 9, 2024

https://doi.org/10.1021/acsami.3c18623

toward halide segregation as an intrinsic material property. Thus, understanding the mixing behavior, starting from the material growth, of mixed iodide−bromide perovskites can help to elucidate these issues further.

For dynamic processes like thin-film growth, in situ X-ray diffraction studies are a viable tool, which can also be applied in combination with other methods such as in situ photoluminescence measurements.[18] In this work, an in situ X-ray analysis of mixed-halide perovskites ($\mathrm{MAPb(Br}_x\mathrm{I}_{1-x})_3$) is provided, including not only halide segregation during light exposure but also focusing on tracking their crystallization from the precursor solution to the final film during the fabrication process. A tendency to segregate is consistent with the distinct growth behavior of mixed-halide thin films, where the crystallization pathways are observed to be different for iodide- and bromide-rich phases, leading to segregated growth and the formation of a mixed-halide perovskite phase only during thermal annealing. A pure bromide perovskite phase crystallizes first, already during spin coating, while the iodide fraction is converted only upon sample annealing via a solvent complex as an intermediate stage and then intermixes into the bromide-rich perovskite phase. Separate crystallization sequences and intermixing of halides upon heat treatment are consistently observed for different thin-film fabrication protocols.

■ RESULTS AND DISCUSSION

Mixing Behavior and Phase Segregation. Mixed-halide perovskite thin films of the composition range $\mathrm{MAPb(Br}_x\mathrm{I}_{1-x})_3$ were prepared using spin coating, including two different methods: the lead acetate route[19] and the gas-quenching technique[20] with a nitrogen flow (details in the Experimental Details). For the bromide ratio x, six values were chosen: 0, 0.2, 0.4, 0.6, 0.8, and 1, with 0 and 1 marking the pure iodide and pure bromide perovskites, respectively. For both methods (compare Figures S1 and S2), in the absence of light, the mixed-halide thin films exhibited a single mixed perovskite phase, which appeared to contain a macroscopically homogeneous mixture of halides.

As reported previously,[1] an expected shift of the perovskite Bragg peak is observed with changing mixing ratios of bromide and iodide (Figure 1a). The peak position shifts linearly with the halide ratio, following Vegard's law for binary mixtures.[21] For measurements in the dark, most compositions feature a single yet rather broad peak, indicative of one single mixed-halide phase. Only the mixture with the highest bromide content (80%) shows a shoulder toward higher q-values, which might indicate an already-beginning phase segregation. The double peak observed for MAPbI_3 is due to its tetragonal structure, while all other mixtures exhibit a cubic symmetry.[1]

Upon illumination with a halogen lamp, diffraction peak splitting is observed for all mixed materials, except the one with 20% bromide, where a pronounced peak broadening can be found (dashed lines in Figure 1a). The single-halide materials do not exhibit significant changes in the diffraction pattern upon illumination, indicating a negligible thermal expansion effect, which might occur due to radiative heating by the lamp. The light-induced peak splitting in the mixed materials is characteristic for segregation into iodide- and bromide-rich phases,[5] while the broadening of the signal in the 20% bromide sample at least shows an increase in disorder or a wider variety in unit cell parameters throughout the sample as a result of illumination. This could be attributed to close-lying overlapping diffraction signals, indicating a separation into phases of maximum ±4% bromide content deviation based on converting the peak position spread into concentration.

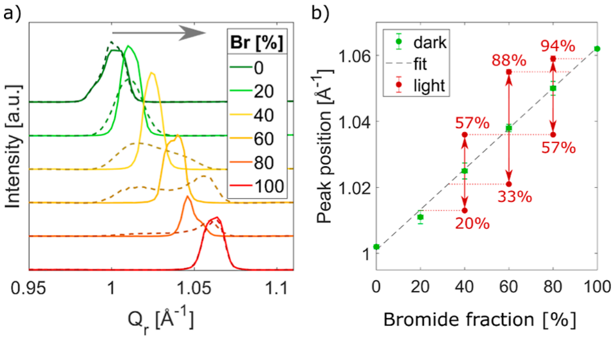

Figure 1. (a) Enlarged section of the radial profiles of GIWAXS reciprocal space maps (incidence angle $\alpha_i = 1°$), highlighting the (100) perovskite diffraction signal. Brightly colored, full lines: fresh samples (fabricated by the lead acetate route) in the dark; dashed, darker lines: the same samples after illumination and phase segregation. (b) Fitted peak positions of the data in (a) with a linear fit following Vegard's law. The red numbers in (b) indicate the final bromide fractions of the segregated phases after light exposure as determined from assuming a linear dependency (horizontal red lines).

Determining the positions of the split peaks after illumination, Vegard's law can be used to calculate the final compositions of the segregated phases, as indicated by the red horizontal dashed lines in Figure 1b. The resulting values for the bromide contents of the maximum segregated phase in each composition are given by the red numbers in the image (more details in Figure S4). Considering the final compositions and assuming that a steady state was reached as suggested by the temporal evolution of the peak positions (Figure S5), the system appears to separate until one of the two phases either has a low bromide content of ≲20% or a high bromide content of ≳90%, which is also consistent with previous reports.[22] It should be noted, though, that the strong illumination might have also increased the temperature of the sample and thus entropic contributions, which tend to favor mixing,[16] possibly inhibiting full segregation into pure-halide phases. This might also contribute to the distinct broadening of the peaks (dashed lines in Figure 1a), indicating a possible distribution of mixed minority phases with slightly differing compositions beside the two segregated majority phases with the distinct compositions given.

By comparing GIWAXS reciprocal space maps, i.e., diffraction patterns as a function of q_{xy} and q_z, of thin films with different mixing ratios before and after illumination (Figure 2, more mixing ratios in Figure S2), it is apparent that the degree of orientation depends only on the mixing ratio. Mixtures with higher bromide content have an increased degree of orientational order along the vertical axis, as indicated by spotlike diffraction signals in the respective reciprocal space maps, as opposed to more ringlike features for more randomly oriented iodide-rich compositions. This finding is generally true for samples fabricated by both the lead acetate fabrication route and the gas-quenching technique, while the gas-quenching method overall produces thin films with a slightly higher orientational order (compare Figure S1). The increasing orientational order of methylammonium-based perovskite materials upon bromide incorporation is likely a general motif, which has been reported in literature before.[23]

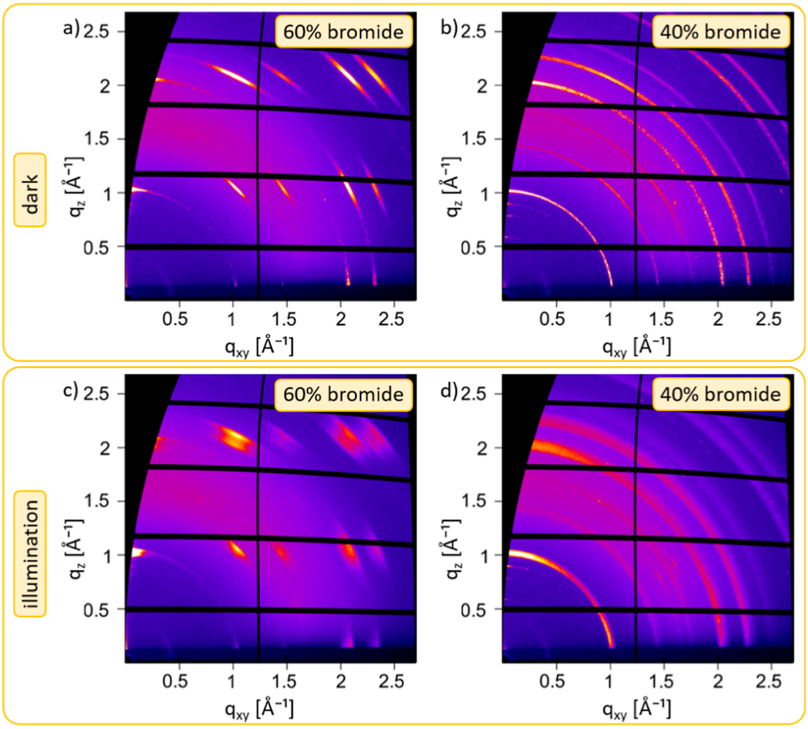

Figure 2. Reciprocal space maps of samples fabricated by the lead acetate route before (a,b) and after (c,d) illumination of thin films with 60% (a,c) and 40% (b,d) of bromide content. A clear peak splitting can be observed after illumination, but the orientational order is retained.

The azimuthal intensity plots in Figure S3 visualize the orientational order of the different mixtures for both fabrication methods, similar to established literature.[24,25]

The degree of orientation does not change upon halide segregation such that both split peaks have the same orientation as the pristine samples (Figure 2c,d). This behavior is consistent with halide segregation occurring via ion migration in the existing perovskite crystallites instead of recrystallization or via amorphous phases.

For the time scale of the segregation with the present setup, 10−15 min was enough to reach a stable state in which the diffraction pattern did not visibly change anymore. Demixing was monitored by real-time GIWAXS (Figure S5, details in the experimental section) and observed to take place gradually, indicated by two closer lying diffraction peaks in the early stages of phase segregation, which move further apart until the equilibrium positions corresponding to the final segregated phase compositions are reached. Variation of the X-ray incidence angle and thus the penetration depth (Figure S6) reveals that the bromide-rich phase seems to be located closer to the surface of the sample, while consequently, the iodide-rich phase is located away from the surface and closer to the substrate.

These findings are consistent with current literature,[22,26] yet hints as to why mixed-halide perovskite thin films behave this way might be found already in their fabrication and crystallization pathway. Thus, the following two sections will focus on the perovskite phase formation during two different thin-film fabrication protocols, featuring first the rather simple gas-quenching technique,[20] followed by the slightly more sophisticated lead acetate route.[19] Details of the fabrication procedures can be found in the experimental section.

Thin-Film Crystallization via Nitrogen Gas Quenching. In situ GIWAXS was used to investigate thin-film growth and crystallization in real time to connect these findings to the mixing and segregation behavior. GIWAXS was recorded during the spin coating process as well as during the annealing process of the mixed-halide thin films for both fabrication routes. The findings via the gas-quenching route will be discussed first due to the simplicity of the process,[20] reducing influences such as antisolvents, additives, or unbalanced stoichiometries on film growth. Afterward, they will be compared to the results of the lead acetate route, which achieves similar final films but via different crystallization sequences.

For the gas-quenching route, the pure $MAPbI_3$ composition first forms the solvent complex $MA_2Pb_3I_8{\cdot}2DMSO$ during spin coating,[27] marked by white crosses in Figure 3a, which shows the evolution of the radial intensities of the reciprocal space maps during the film formation process. The corresponding integrated intensities of signature peaks in Figure 4a,e show that thermal annealing converts the intermediate solvent complex to the perovskite phase, which is marked by yellow circles in Figure 3. Conversely, the pure $MAPbBr_3$ composition (Figures 3b and 4d,h) directly crystallizes in the perovskite phase and does not change significantly during annealing.

For mixed films, the distinct signals of the bromide-based perovskite structure also appear during spin coating (Figures 4b,c and S8). From the peak position, this seems to be an almost pure bromide perovskite phase (Figure S10). Increasing the iodide fraction within the composition results in higher scattering signals from the $MA_2Pb_3I_8{\cdot}2DMSO$ solvent complex, which evolve during the annealing (Figures 3c,d and 4b,f,g). With low iodide content (≥60% bromide), the $MA_2Pb_3I_8{\cdot}2DMSO$ phase is not observed during the spin coating but only temporarily in minor amounts during thermal treatment (also compare Figures S7−S9). In the course of the annealing procedure, the signals of this solvent complex phase

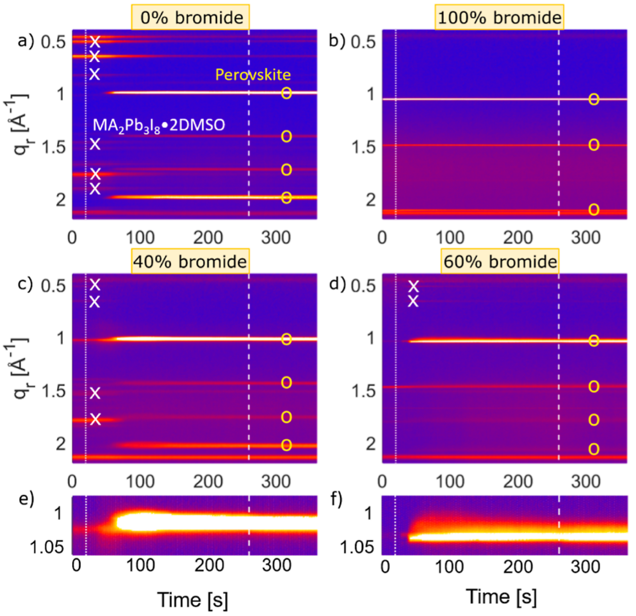

Figure 3. Intensity maps from radial profiles of GIWAXS reciprocal space maps as a function of time during sample annealing for samples fabricated via the N_2 gas-quenching route. (a) 0% bromide/pure $MAPbI_3$, (b) 100% bromide, (c) 40% bromide, and (d) 60% bromide. White crosses mark the $MA_2Pb_3I_8\cdot 2DMSO$ phase, while perovskite is marked with yellow circles. (e,f) Magnified view of the region around $q = 1$ Å^{-1} in (c,d). Vertical white dotted lines: start of heating; dashed lines: heat source turned off. More mixing ratios can be found in Figure S7.

vanish, together with a shift of the perovskite peaks toward lower q-values, indicating an increase of the unit cell size, which reflects the inclusion of the larger iodide ions into the perovskite structure (Figure S10). A similar type of sequential crystallization with changing halide composition has been reported before for all-inorganic perovskite structures.[28] Additionally, for the mixed compositions, the perovskite peaks not only shift upon annealing but also widen in the early stages of annealing, indicative of an increased amount of disorder, which might reflect a smaller domain size or slight differences in the unit cell size throughout the sample (Figure S11). This might also be related to a partial dissolution of the bromide-rich domains upon the start of iodide intermixing. During prolonged annealing, the peak width is reduced again, suggesting a more homogeneous mixing of halides with a more uniform distribution of unit cell sizes. This can be seen clearly in the enlarged sections of the profile evolution of the perovskite (100) signal in Figure 3e,f, where an initial higher-q peak is followed by a broader peak shifted to lower q, indicating the increase in the unit cell size upon iodide inclusion as well as an increase in disorder in the early stages of mixed perovskite formation.

A direct crystallization of $MAPbBr_3$ perovskite without intermediate stages or need for annealing has been observed before and might be ascribed to the higher bonding strength between Pb^{2+} and Br^- compared to that of the I^- anion[29−31] or a reduced stability of the lead bromide solvent adducts.[32] For the iodide compound $MAPbI_3$, the growth via intermediate solvent complexes is well reported.[33] Interestingly, for the mixed-halide samples, both processes, direct $MAPbBr_3$ crystallization and $MAPbI_3$ formation via intermediates, were observed simultaneously, leading to the initial growth of a bromide-rich perovskite phase and subsequent intermixing and inclusion of iodide after thermal conversion of the iodide-based solvent complex.

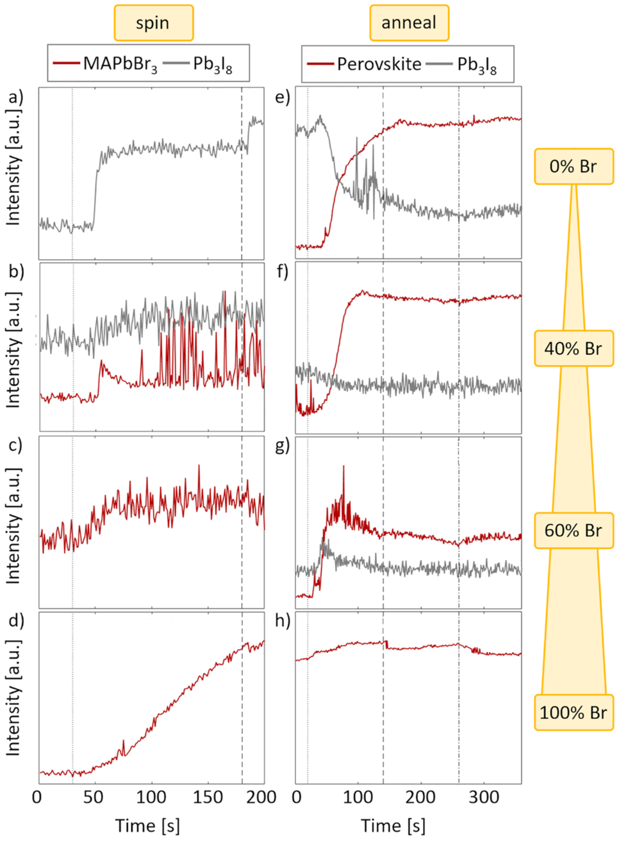

Figure 4. Normalized integrated peak intensities from radial profiles of GIWAXS reciprocal space maps as a function of time during (a−d) spin coating and (e−h) annealing for samples fabricated via the N_2 gas-quenching route. (a,e) 0% bromide/pure $MAPbI_3$, (b,f) 40% bromide, (c,g) 60% bromide, and (d,h) 100% bromide. Legend colors apply for all samples, except during spin coating, where the red curve marks the Br-rich perovskite phase and in the annealing data, the mixed perovskite phase. A list of the signature peaks used for all phases can be found in Table S1. Vertical dotted lines in (a−d): start of spinning; dashed lines: end of spinning. Vertical dotted lines in (e−h): start of heating; dashed lines: reduction of heating power; dotted−dashed lines: heat source turned off. Pb_3I_8 in this case is short for the DMSO-based $MA_2Pb_3I_8\cdot 2DMSO$ solvent complex. More mixing ratios can be found in Figure S9.

Thin-Film Crystallization via the Lead Acetate Route.

The above investigations were done for thin films fabricated by nitrogen-gas quenching, which will now be compared to the lead acetate route, with which the samples subjected to light-induced segregation described in the first section have been fabricated. This method is often used to tune the thin-film microstructure[19] since lead acetate has been observed to assist the formation of perovskites in various compositions.[34] The process was also investigated in real time to assess the universality of the crystallization behavior over different fabrication protocols.

The overall crystallization behavior during the lead acetate route was generally similar to the nitrogen quenching: iodide- and bromide-based phases followed their separate crystallization sequences in parallel, and a mixed perovskite phase was formed only upon annealing.

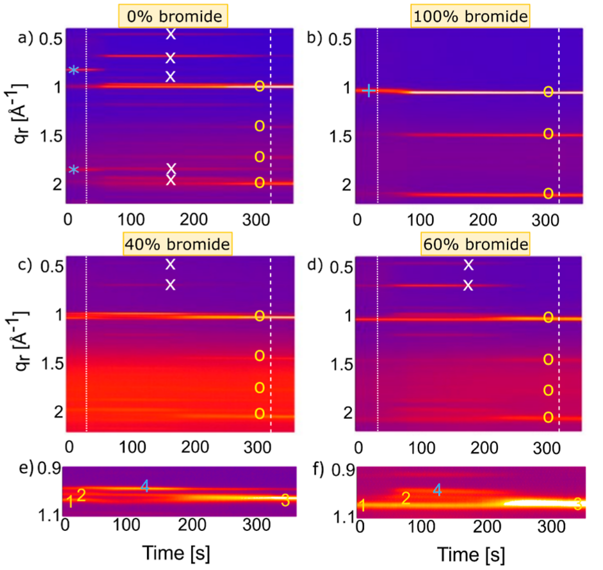

Figure 5. Intensity maps from radial profiles of GIWAXS reciprocal space maps as a function of time during sample annealing for samples fabricated via the lead acetate route. (a) 0% bromide/pure $MAPbI_3$, (b) 100% bromide, (c) 40% bromide, and (d) 60% bromide. White crosses mark the $MA_2Pb_3I_8 \cdot 2DMF$ phase, while perovskite is marked with yellow circles. Blue asterisks mark hexagonal $MAPbI_3$ in (a) and blue plus signs indicate the layered MA_2PbBr_4 phase in (b). Vertical white dotted lines: start of heating; dashed lines: heat source turned off. (e,f) Enlarged view of the region around q = 1 Å^{-1} in (c,d). Numbers in (e,f) indicate bromide-rich (1), iodide-rich (2), and mixed (3) perovskite phases and the layered MA_2PbBr_4 phase (4).

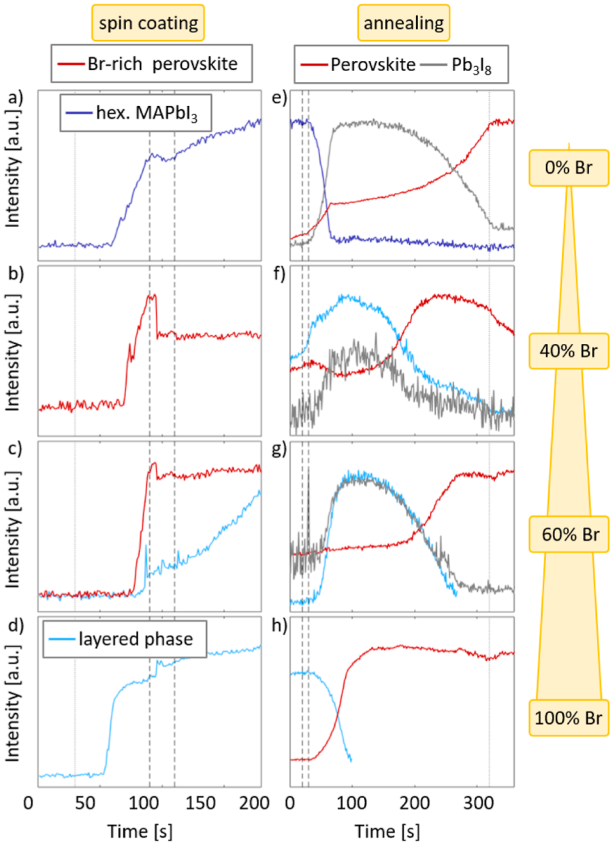

Figure 6. Normalized integrated peak intensities from radial profiles of GIWAXS reciprocal space maps as a function of time during (a−d) spin coating and (e−h) annealing for samples fabricated via the lead acetate route. (a,e) 0% bromide/pure $MAPbI_3$, (b,f) 40% bromide, (c,g) 60% bromide, and (d,h) 100% bromide. Legend colors apply for all samples, except during spin coating, where the red curve marks the Br-rich perovskite phase and in the annealing data, the mixed perovskite. A list of the signature peaks used for all phases can be found in Table S1. Vertical dotted lines in (a−d): start of spinning; dashed lines: end of spinning/end of air flow. Vertical dashed lines in (e−h): start of heating/reduction of heating power; dotted lines: heat source turned off. Pb_3I_8 in this case is short for the DMF-based $MA_2Pb_3I_8 \cdot 2DMF$ intermediate solvent complex.

$MAPbI_3$ was formed via a structurally similar solvent intermediate as for the gas-quenching method, in this case, DMF-based $MA_2Pb_3I_8 \cdot 2DMF$,[35] since DMSO was absent in the precursor solutions for this fabrication route (Figures 5a and 6e). Due to the highly nonstoichiometric nature of the precursor solution with its 3:1 ratio of MA/Pb, hexagonal $MAPbI_3$ could be observed during spin coating (Figures 5a and 6a), which has only been found to occur with a large methylammonium and halide excess.[36] This hexagonal $MAPbI_3$ phase,[37] according to the positions of its diffraction signals (blue asterisks in Figure 5a), seems to have a similar structure as the well-known $FAPbI_3$ δ-phase[38] containing linear chains of lead-halide octahedra. Via a complex three-phase conversion sequence involving the $MA_2Pb_3I_8 \cdot 2DMF$ solvent complex phase, a $MAPbI_3$ perovskite phase is established during prolonged thermal annealing (Figure 6e).

Bromide perovskite, similar to the gas-quenching method, was crystallized without forming solvent complexes (Figures 5b and 6d,h), but this time, a crystalline precursor phase was formed during spin coating (marked by blue plus signs in Figures 5b and S12), which was then transformed to the $MAPbBr_3$ perovskite structure during annealing. Due to its slightly lower q diffraction signal of around 1.038 Å^{-1} (as compared to that of $MAPbBr_3$ at q = 1.06 Å^{-1}[39]), which indicates a larger unit cell than that of the $MAPbBr_3$ perovskite, it is suspected to be a layered MA_2PbBr_4 phase. This kind of structure is only expected to form with a pronounced lead deficiency[40] in the precursor solution, which was indeed present here due to a 3-fold excess of MAX in the formulation. The conversion of this layered structure into perovskite is illustrated by reciprocal space maps at representative time instances in Figure S12. The formation of a layered intermediate phase might also be linked to the higher general tendency of bromide-based compositions to form well-oriented perovskite phases since their growth might be templated by similar locally formed nuclei of the layered phase, which are generally well-oriented.[41]

Similar to the gas-quenching route, in the mixed samples, iodide and bromide phases evolve separately with and without solvent complex intermediates, respectively. Only at the later stages of annealing do they merge into a single, macroscopically mixed perovskite phase. All mixed samples already exhibit a perovskite phase during spin coating (Figure S13), which, according to its peak position of about q = 1.06 Å^{-1}, is a bromide-based perovskite phase.[39] During annealing, the layered MA_2PbBr_4 phase and the $MA_2Pb_3I_8 \cdot 2DMF$ solvent complex evolve simultaneously and are transformed into the perovskite phase (Figures 5c−f and 6f,g). Although Figure 6 displays the perovskite phase as a single graph, a close look at the diffraction peak and its development (Figure 5e,f) reveals initially two close-lying peaks (marked by 1 and 2)

https://doi.org/10.1021/acsami.3c18623

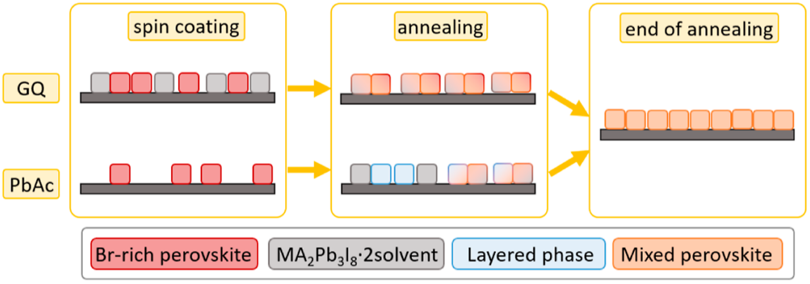

Figure 7. Schematic depiction of the crystallization behavior of mixed-halide perovskite thin films. GQ: gas quenching; PbAc: lead acetate route. Bromide-rich perovskite phase forms already during spin coating, while the iodide fraction forms intermediate solvent complexes based on DMF or DMSO. During annealing, the mixed-halide perovskite phase is established.

corresponding to two separate bromide- and iodide-rich perovskite phases, which merge into one significantly broader diffraction peak with an intermediate q-value (marked as 3). The signal of the layered phase (marked as 4) disappears simultaneously with this process, indicating its conversion to the perovskite phase.

Thus, the separate growth of iodide and bromide perovskites with subsequent halide mixing appears to be a general pattern, which is retained over different fabrication routes.

The observed growth behavior is consistent with the properties of the final thin films investigated in section *a*: first, it might explain the dependence of orientational order on the bromide content since the bromide perovskite phase templates oriented growth, which is retained when intermixing iodide to a certain extent depending on the mixing ratio. Second, the parallel crystallization sequences hint toward a segregation tendency of mixed iodide–bromide perovskites. This leads to a bromide-based perovskite matrix, established at room temperature, which is interspersed with iodide only upon annealing, resulting in a macroscopically uniform mixture that might, however, still contain locally enriched regions of iodide or bromide.

■ CONCLUSIONS

In summary, the detailed route of mixed-halide perovskite thin-film growth (simplified schematic depiction in Figure 7) was revealed and was connected to the mixing and segregation behavior. A gradual segregation into bromide- and iodide-rich domains was found upon illumination of thin films, consistent with previous reports. During the deposition of these thin films, bromide- and iodide-based phases follow separate crystallization sequences and only form a mixed-halide perovskite phase upon annealing. While the iodide-based fraction crystallizes via intermediate solvent complexes, these are not observed for the bromide fraction, which crystallizes directly as a perovskite phase and is intermixed with iodide during thermal treatment. Using highly nonstoichiometric precursor solutions, like in the lead acetate route, generates low-dimensional phases as an intermediate stage, but the general motif of halide-segregated crystallization sequences and the formation of a mixed perovskite only upon thermal annealing seems to be universal.

This distinct growth behavior of each halide perovskite phase evolving separately, which is retained even for different fabrication methods, might be a further piece in the puzzle of halide segregation, its driving forces, and mechanisms. The fact that intermixing happens only during thermal treatment reflects the entropic contribution to halide mixing, but the intrinsic tendency to segregate manifests in a separate growth sequence for the bromide- and iodide-based fractions of the material. This could, in turn, be the cause for small inhomogeneities in the final film due to imperfect mixing, which could then serve as nucleation centers for halide segregation. The segregated growth process might thus be linked to potential seeds for light-induced halide segregation. Therefore, future research might be dedicated to establishing fabrication methods for mixed-halide perovskite thin films, which already promote halide mixing during crystal growth and prevent segregated crystallization sequences.

■ EXPERIMENTAL DETAILS

Halide Segregation Experiments. Perovskite thin films were prepared by the lead acetate route, as described below. Halide segregation experiments were conducted at beamline *P*23, DESY. The experiments took place in a nitrogen atmosphere, and the beam energy was varied from 12,974 to 13,974 eV. Illumination was achieved by a halogen lamp at a power density of $0.9\ \frac{\mathrm{W}}{\mathrm{cm}^2}$ for 50–100 min using a silver reflector to reduce heating of the sample. The maximum temperature of the sample during prolonged illumination was about 65 °C. The incidence angle of the X-rays was varied from 0 to 1°, and for real-time observations, it was fixed at 1°. The beam size was 300 × 100 μm and the sample-to-detector distance was 350 mm. The instrumental broadening for the described setup was estimated to be on the order of magnitude of 0.01 Å^{-1} around the position of $q = 1$ Å^{-1}, where the perovskite signal was located.

Thin-Film Fabrication via the Nitrogen Gas-Quenching Route. Precursor solutions were prepared from PbI_2 (AnhydroBeads, 99.999%, *Sigma-Aldrich*), $PbBr_2$ (99.999%, *Sigma-Aldrich*), MAI (anhydrous, 99.99%, *dyenamo*), and MABr (anhydrous, 99.99%, *dyenamo*) in a 4:1 v/v mixture of DMF (biotech. grade, ≥99.9%, *Sigma-Aldrich*) and DMSO (anhydrous, ≥99.9%, *Sigma-Aldrich*) dissolved in a nitrogen atmosphere with a concentration of 1.4 M using stoichiometric precursor amounts. Thin-film deposition took place in a specifically designed deposition system,[42] which allowed us to simultaneously measure GIWAXS at beamline P08,[43] DESY. The films were spin-coated at 3000 rpm for 150 s, while after 15 s, a nitrogen flow was directed at the sample to establish gas-quenching.[20] Thin films were annealed at 100 °C for 4–10 min.

Thin-Film Fabrication via the Lead Acetate Route. Perovskite films were fabricated by adapting the lead acetate route previously described elsewhere.[19] MAI and MABr (>99.99%, *Great Cell Solar*) were dissolved in a drybox (relative humidity <0.4%) in *N*,*N*-dimethylformamide (DMF, anhydrous, *Sigma-Aldrich*) to a 42 wt % concentration, followed by the addition of hypophosphorous acid (HPA, 50:50 vol % in water, *Alfa Aesar*, 1.7 μL per 63 μmol methylammonium halide). Appropriate amounts of methylammonium halide solution (halide/lead 3:1) were either added directly to lead acetate trihydrate (>99%, *Sigma-Aldrich*) or mixed by volume beforehand to form mixtures of halides. The final solutions were spin-coated on bare or ITO-coated glass (soda–lime glass, precleaned with acetone, isopropanol, and oxygen plasma) at 2000 rpm for 60 s in a

DMF-rich atmosphere. Directly at the end of the spin coating, a compressed dry air flow was directed at the as-deposited thin film for 20 s. After being dried for 5 min in dry air, the samples were annealed for 5 min at 100 °C in the same environment.

In Situ GIWAXS. For real-time experiments[44] at DESY beamline P08,[43] the beam energy was 17,987 eV, the incidence angle was 0.5°, and the beam size was 500 × 200 μm. A *PerkinElmer XRD 1621* detector with a spatial resolution of 200 μm was used to record two-dimensional diffraction patterns with an integration time of 0.1 s and a sample-to-detector distance of 700 mm. Both the nitrogen gas-quenching route and the lead acetate preparation route, as described in the previous sections, were performed while measuring in situ GIWAXS using the same measurement parameters and the same custom deposition setup.[42]

ASSOCIATED CONTENT

Supporting Information

The Supporting Information is available free of charge at https://pubs.acs.org/doi/10.1021/acsami.3c18623.

X-ray data and graphics (PDF)

AUTHOR INFORMATION

Corresponding Author

Lena Merten − *Institute of Applied Physics, University of Tübingen, 72076 Tübingen, Germany;* orcid.org/0000-0002-9364-6948; Email: lena.merten@student.uni-tuebingen.de

Authors

Timo Eberle − *Institute of Applied Physics, University of Tübingen, 72076 Tübingen, Germany*
Ekaterina Kneschaurek − *Institute of Applied Physics, University of Tübingen, 72076 Tübingen, Germany*
Niels Scheffczyk − *Institute of Applied Physics, University of Tübingen, 72076 Tübingen, Germany*
Paul Zimmermann − *Institute of Applied Physics, University of Tübingen, 72076 Tübingen, Germany*
Ivan Zaluzhnyy − *Institute of Applied Physics, University of Tübingen, 72076 Tübingen, Germany;* orcid.org/0000-0001-5946-2777
Azat Khadiev − *Deutsches Elektronen-Synchrotron DESY, 22607 Hamburg, Germany*
Florian Bertram − *Deutsches Elektronen-Synchrotron DESY, 22607 Hamburg, Germany*
Fabian Paulus − *Institute for Materials Chemistry, Leibniz Institute for Solid State and Materials Research Dresden (IFW), 01069 Dresden, Germany; Center for Advancing Electronics Dresden (cfaed), Technische Universität Dresden, 01069 Dresden, Germany;* orcid.org/0000-0001-7068-440X
Alexander Hinderhofer − *Institute of Applied Physics, University of Tübingen, 72076 Tübingen, Germany;* orcid.org/0000-0001-8152-6386
Frank Schreiber − *Institute of Applied Physics, University of Tübingen, 72076 Tübingen, Germany;* orcid.org/0000-0003-3659-6718

Complete contact information is available at: https://pubs.acs.org/10.1021/acsami.3c18623

Author Contributions

Samples were prepared by TE and LM (samples for the gas-quenching route), EK and LM (samples for the lead acetate route), and FP (samples for halide segregation as well as solutions for the lead acetate route). The data were measured by EK, NS, PZ, and AH (halide segregation), TE and LM (real-time gas-quenching), and EK and LM (real-time lead acetate route). Data evaluation was done by TE (real-time gas-quenching) and LM (all others), while the manuscript was written by LM with the support of all authors. IZ provided reference measurements and helpful discussions. AK assisted in using beamline P23 at DESY and establishing the setup, while FB supported using DESY beamline P08. AH and FS supervised the project.

Notes

The authors declare no competing financial interest.

ACKNOWLEDGMENTS

The authors gratefully acknowledge funding by the DFG in the framework of the Priority Program "Perovskite Semiconductors: From Fundamental Properties to Devices" (SPP 2196) for grant no. LE 747/64-1 as well as the BMBF/ErUM-pro no. 05K19VTA. We acknowledge DESY (Hamburg, Germany), a member of the Helmholtz Association HGF, for the provision of experimental facilities. Parts of this research were carried out at PETRA III, and we would like to thank Dmitry Novikov for assistance in using beamline P23. Beamtime was allocated for proposals I-20210276, I-20220453, and I20221269.

REFERENCES

(1) Noh, J. H.; Im, S. H.; Heo, J. H.; Mandal, T. N.; Seok, S. I. Chemical Management for Colorful, Efficient, and Stable Inorganic-Organic Hybrid Nanostructured Solar Cells. *Nano Lett.* **2013**, *13*, 1764−1769.

(2) Chen, Y.; Motti, S. G.; Oliver, R. D. J.; Wright, A. D.; Snaith, H. J.; Johnston, M. B.; Herz, L. M.; Filip, M. R. Optoelectronic Properties of Mixed Iodide-Bromide Perovskites from First-Principles Computational Modeling and Experiment. *J. Phys. Chem. Lett.* **2022**, *13*, 4184−4192.

(3) Brinkmann, K. O.; Becker, T.; Zimmermann, F.; Kreusel, C.; Gahlmann, T.; Theisen, M.; Haeger, T.; Olthof, S.; Tückmantel, C.; Günster, M.; Maschwitz, T.; Göbelsmann, F.; Koch, C.; Hertel, D.; Caprioglio, P.; Peña-Camargo, F.; Perdigón-Toro, L.; Al-Ashouri, A.; Merten, L.; Hinderhofer, A.; Gomell, L.; Zhang, S.; Schreiber, F.; Albrecht, S.; Meerholz, K.; Neher, D.; Stolterfoht, M.; Riedl, T. Perovskite-Organic Tandem Solar Cells with Indium Oxide Interconnect. *Nature* **2022**, *604*, 280−286.

(4) Braly, I. L.; Stoddard, R. J.; Rajagopal, A.; Uhl, A. R.; Katahara, J. K.; Jen, A. K.-Y.; Hillhouse, H. W. Current-Induced Phase Segregation in Mixed Halide Hybrid Perovskites and its Impact on Two-Terminal Tandem Solar Cell Design. *ACS Energy Lett.* **2017**, *2*, 1841−1847.

(5) Hoke, E. T.; Slotcavage, D. J.; Dohner, E. R.; Bowring, A. R.; Karunadasa, H. I.; McGehee, M. D. Reversible Photo-Induced Trap Formation in Mixed-Halide Hybrid Perovskites for Photovoltaics. *Chem. Sci.* **2015**, *6*, 613−617.

(6) Yoon, S. J.; Draguta, S.; Manser, J. S.; Sharia, O.; Schneider, W. F.; Kuno, M.; Kamat, P. V. Tracking Iodide and Bromide Ion Segregation in Mixed Halide Lead Perovskites during Photoirradiation. *ACS Energy Lett.* **2016**, *1*, 290−296.

(7) Bischak, C. G.; Hetherington, C. L.; Wu, H.; Aloni, S.; Ogletree, D. F.; Limmer, D. T.; Ginsberg, N. S. Origin of Reversible Photoinduced Phase Separation in Hybrid Perovskites. *Nano Lett.* **2017**, *17*, 1028−1033.

(8) Chen, Z.; Brocks, G.; Tao, S.; Bobbert, P. A. Unified Theory for Light-Induced Halide Segregation in Mixed Halide Perovskites. *Nat. Commun.* **2021**, *12*, 2687.

(9) Brivio, F.; Caetano, C.; Walsh, A. Thermodynamic Origin of Photoinstability in the $CH_3NH_3Pb(I_{1-x}Br_x)_3$ Hybrid Halide Perovskite Alloy. *J. Phys. Chem. Lett.* **2016**, *7*, 1083−1087.

(10) Bischak, C. G.; Wong, A. B.; Lin, E.; Limmer, D. T.; Yang, P.; Ginsberg, N. S. Tunable Polaron Distortions Control the Extent of Halide Demixing in Lead Halide Perovskites. *J. Phys. Chem. Lett.* **2018**, *9*, 3998−4005.

(11) Mao, W.; Hall, C. R.; Bernardi, S.; Cheng, Y. B.; Widmer-Cooper, A.; Smith, T. A.; Bach, U. Light-Induced Reversal of Ion Segregation in Mixed-Halide Perovskites. *Nat. Mater.* **2021**, *20*, 55−61.

(12) Kerner, R. A.; Xu, Z.; Larson, B. W.; Rand, B. P. The Role of Halide Oxidation in Perovskite Halide Phase Separation. *Joule* **2021**, *5*, 2273−2295.

(13) Knight, A. J.; Wright, A. D.; Patel, J. B.; McMeekin, D. P.; Snaith, H. J.; Johnston, M. B.; Herz, L. M. Electronic Traps and Phase Segregation in Lead Mixed-Halide Perovskite. *ACS Energy Lett.* **2019**, *4*, 75−84.

(14) Knight, A. J.; Patel, J. B.; Snaith, H. J.; Johnston, M. B.; Herz, L. M. Trap States, Electric Fields, and Phase Segregation in Mixed-Halide Perovskite Photovoltaic Devices. *Adv. Energy Mater.* **2020**, *10*, 1903488.

(15) Suchan, K.; Just, J.; Beblo, P.; Rehermann, C.; Merdasa, A.; Mainz, R.; Scheblykin, I. G.; Unger, E. Multi-Stage Phase-Segregation of Mixed Halide Perovskites under Illumination: A Quantitative Comparison of Experimental Observations and Thermodynamic Models. *Adv. Funct. Mater.* **2022**, *33*, 2206047.

(16) Knight, A. J.; Herz, L. M. Preventing Phase Segregation in Mixed-Halide Perovskites: a Perspective. *Energy Environ. Sci.* **2020**, *13*, 2024−2046.

(17) Barker, A. J.; Sadhanala, A.; Deschler, F.; Gandini, M.; Senanayak, S. P.; Pearce, P. M.; Mosconi, E.; Pearson, A. J.; Wu, Y.; Srimath Kandada, A. R.; Leijtens, T.; De Angelis, F.; Dutton, S. E.; Petrozza, A.; Friend, R. H. Defect-Assisted Photoinduced Halide Segregation in Mixed-Halide Perovskite Thin Films. *ACS Energy Lett.* **2017**, *2*, 1416−1424.

(18) Mrkyvkova, N.; Held, V.; Nádaždy, P.; Subair, R.; Majkova, E.; Jergel, M.; Vlk, A.; Ledinsky, M.; Kotlár, M.; Tian, J.; Siffalovic, P. Combined in Situ Photoluminescence and X-ray Scattering Reveals Defect Formation in Lead-Halide Perovskite Films. *J. Phys. Chem. Lett.* **2021**, *12*, 10156−10162.

(19) Sun, Q.; Fassl, P.; Becker-Koch, D.; Bausch, A.; Rivkin, B.; Bai, S.; Hopkinson, P. E.; Snaith, H. J.; Vaynzof, Y. Role of Microstructure in Oxygen Induced Photodegradation of Methylammonium Lead Triiodide Perovskite Films. *Adv. Energy Mater.* **2017**, *7*, 1700977.

(20) Brinkmann, K. O.; He, J.; Schubert, F.; Malerczyk, J.; Kreusel, C.; van gen Hassend, F.; Weber, S.; Song, J.; Qu, J.; Riedl, T. Extremely Robust Gas-Quenching Deposition of Halide Perovskites on Top of Hydrophobic Hole Transport Materials for Inverted (p-i-n) Solar Cells by Targeting the Precursor Wetting Issue. *ACS Appl. Mater. Interfaces* **2019**, *11*, 40172−40179.

(21) Vegard, L. Die Konstitution der Mischkristalle und die Raumfüllung der Atome. *Z. Phys.* **1921**, *5*, 17−26.

(22) Halford, G. C.; Deng, Q.; Gomez, A.; Green, T.; Mankoff, J. M.; Belisle, R. A. Structural Dynamics of Metal Halide Perovskites during Photoinduced Halide Segregation. *ACS Appl. Mater. Interfaces* **2022**, *14*, 4335−4343.

(23) Zou, Y.; Bai, X.; Kahmann, S.; Dai, L.; Yuan, S.; Yin, S.; Heger, J. E.; Schwartzkopf, M.; Roth, S. V.; Chen, C.-C.; Zhang, J.; Stranks, S. D.; Friend, R. H.; Müller-Buschbaum, P. A Practical Approach Toward Highly Reproducible and High-Quality Perovskite Films Based on an Aging Treatment. *Adv. Mater.* **2023**, *36*, 1521−4095.

(24) Zhang, Y.; Wang, P.; Tang, M.-C.; Barrit, D.; Ke, W.; Liu, J.; Luo, T.; Liu, Y.; Niu, T.; Smilgies, D.-M.; Yang, Z.; Liu, Z.; Jin, S.; Kanatzidis, M. G.; Amassian, A.; Liu, S. F.; Zhao, K. Dynamical Transformation of Two-Dimensional Perovskites with Alternating Cations in the Interlayer Space for High-Performance Photovoltaics. *J. Am. Chem. Soc.* **2019**, *141*, 2684−2694.

(25) Wang, S.; Yang, T.; Yang, Y.; Du, Y.; Huang, W.; Cheng, L.; Li, H.; Wang, P.; Wang, Y.; Zhang, Y.; Ma, C.; Liu, P.; Zhao, G.; Ding, Z.; Liu, S. F.; Zhao, K. In Situ Self-Elimination of Defects via Controlled Perovskite Crystallization Dynamics for High-Performance Solar Cells. *Adv. Mater.* **2023**, *35*, 1521−4095.

(26) Cappel, U. B.; Svanström, S.; Lanzilotto, V.; Johansson, F. O. L.; Aitola, K.; Philippe, B.; Giangrisostomi, E.; Ovsyannikov, R.; Leitner, T.; Föhlisch, A.; Svensson, S.; Mårtensson, N.; Boschloo, G.; Lindblad, A.; Rensmo, H. Partially Reversible Photoinduced Chemical Changes in a Mixed-Ion Perovskite Material for Solar Cells. *ACS Appl. Mater. Interfaces* **2017**, *9*, 34970−34978.

(27) Cao, J.; Jing, X.; Yan, J.; Hu, C.; Chen, R.; Yin, J.; Li, J.; Zheng, N. Identifying the Molecular Structures of Intermediates for Optimizing the Fabrication of High-Quality Perovskite Films. *J. Am. Chem. Soc.* **2016**, *138*, 9919−9926.

(28) Fan, Y.; Fang, J.; Chang, X.; Tang, M.-C.; Barrit, D.; Xu, Z.; Jiang, Z.; Wen, J.; Zhao, H.; Niu, T.; Smilgies, D.-M.; Jin, S.; Liu, Z.; Li, E. Q.; Amassian, A.; Liu, S. F.; Zhao, K. Scalable Ambient Fabrication of High-Performance $CsPbI_2Br$ Solar Cells. *Joule* **2019**, *3*, 2485−2502.

(29) Yoon, S. J.; Stamplecoskie, K. G.; Kamat, P. V. How Lead Halide Complex Chemistry Dictates the Composition of Mixed Halide Perovskites. *J. Phys. Chem. Lett.* **2016**, *7*, 1368−1373.

(30) Xie, Y.-M.; Ma, C.; Xu, X.; Li, M.; Ma, Y.; Wang, J.; Chandran, H. T.; Lee, C.-S.; Tsang, S.-W. Revealing the Crystallization Process and Realizing Uniform 1.8 eV MA-Based Wide-Bandgap Mixed-Halide Perovskites via Solution Engineering. *Nano Res.* **2019**, *12*, 1033−1039.

(31) Pistor, P.; Burwig, T.; Brzuska, C.; Weber, B.; Fränzel, W. Thermal Stability and Miscibility of Co-Evaporated Methyl ammonium Lead Halide ($MAPbX_3$, X = I, Br, Cl) Thin Films Analysed by *in situ* X-ray Diffraction. *J. Mater. Chem. A* **2018**, *6*, 11496−11506.

(32) Barrit, D.; Zhang, Y.; Yang, T.; Tang, M.-C.; Li, R.; Smilgies, D.-M.; Frank Liu, S.; Anthopoulos, T. D.; Amassian, A.; Zhao, K. Sequential Formation of Tunable-Bandgap Mixed-Halide Lead-Based Perovskites: In Situ Investigation and Photovoltaic Devices. *Sol. RRL* **2020**, *5*, 2000668.

(33) Rong, Y.; Tang, Z.; Zhao, Y.; Zhong, X.; Venkatesan, S.; Graham, H.; Patton, M.; Jing, Y.; Guloy, A. M.; Yao, Y. Solvent Engineering Towards Controlled Grain Growth in Perovskite Planar Heterojunction Solar Cells. *Nanoscale* **2015**, *7*, 10595−10599.

(34) Xi, J.; Wang, H.; Yuan, J.; Yan, X.; Siffalovic, P.; Tian, J. High-Quality α-$FAPbI_3$ Film Assisted by Lead Acetate for Efficient Solar Cells. *Sol. RRL* **2021**, *5*, 2100747.

(35) Petrov, A. A.; Sokolova, I. P.; Belich, N. A.; Peters, G. S.; Dorovatovskii, P. V.; Zubavichus, Y. V.; Khrustalev, V. N.; Petrov, A. V.; Grätzel, M.; Goodilin, E. A.; Tarasov, A. B. Crystal Structure of DMF-Intermediate Phases Uncovers the Link Between $CH_3NH_3PbI_3$ Morphology and Precursor Stoichiometry. *J. Phys. Chem. C* **2017**, *121*, 20739−20743.

(36) Song, Z.; Watthage, S. C.; Phillips, A. B.; Tompkins, B. L.; Ellingson, R. J.; Heben, M. J. Impact of Processing Temperature and Composition on the Formation of Methylammonium Lead Iodide Perovskites. *Chem. Mater.* **2015**, *27*, 4612−4619.

(37) Thind, A. S.; Huang, X.; Sun, J.; Mishra, R. First-Principles Prediction of a Stable Hexagonal Phase of $CH_3NH_3PbI_3$. *Chem. Mater.* **2017**, *29*, 6003−6011.

(38) Gratia, P.; Zimmermann, I.; Schouwink, P.; Yum, J.-H.; Audinot, J.-N.; Sivula, K.; Wirtz, T.; Nazeeruddin, M. K. The Many Faces of Mixed Ion Perovskites: Unraveling and Understanding the Crystallization Process. *ACS Energy Lett.* **2017**, *2*, 2686−2693.

(39) López, C. A.; Martínez-Huerta, M. V.; Alvarez-Galván, M. C.; Kayser, P.; Gant, P.; Castellanos-Gomez, A.; Fernández-Díaz, M. T.; Fauth, F.; Alonso, J. A. Elucidating the Methylammonium (MA) Conformation in $MAPbBr_3$ Perovskite with Application in Solar Cells. *Inorg. Chem.* **2017**, *56*, 14214−14219.

(40) Petrov, A. A.; Fateev, S. A.; Khrustalev, V. N.; Li, Y.; Dorovatovskii, P. V.; Zubavichus, Y. V.; Goodilin, E. A.; Tarasov, A. B. Formamidinium Haloplumbate Intermediates: The Missing Link in a Chain of Hybrid Perovskites Crystallization. *Chem. Mater.* **2020**, *32*, 7739−7745.

(41) Jahanbakhshi, F.; Mladenović, M.; Kneschaurek, E.; Merten, L.; Gélvez-Rueda, M. C.; Ahlawat, P.; Li, Y.; Dučinskas, A.; Hinderhofer, A.; Dar, M. I.; Tress, W.; Carlsen, B.; Ummadisingu, A.; Zakeeruddin, S. M.; Hagfeldt, A.; Schreiber, F.; Grozema, F. C.; Rothlisberger, U.; Milić, J. V.; Graetzel, M. Unravelling the Structural Complexity and Photophysical Properties of Adamantyl-Based Layered Hybrid Perovskites. *J. Mater. Chem. A* **2020**, *8*, 17732−17740.

(42) Kneschaurek, E.; Hinderhofer, A.; Hofferberth, B.; Scheffczyk, N.; Pithan, L.; Zimmermann, P.; Merten, L.; Bertram, F.; Schreiber, F. Compact Sample Environment for in situ X-ray Scattering during Spin-Coating. *Rev. Sci. Instrum.* **2023**, *94*, 063901.

(43) Seeck, O. H.; Deiter, C.; Pflaum, K.; Bertam, F.; Beerlink, A.; Franz, H.; Horbach, J.; Schulte-Schrepping, H.; Murphy, B. M.; Greve, M.; Magnussen, O. The High-Resolution Diffraction Beamline P08 at PETRA III. *J. Synchrotron Radiat.* **2012**, *19*, 30−38.

(44) Greco, A.; Hinderhofer, A.; Dar, M. I.; Arora, N.; Hagenlocher, J.; Chumakov, A.; Grätzel, M.; Schreiber, F. Kinetics of Ion-Exchange Reactions in Hybrid Organic-Inorganic Perovskite Thin Films Studied by In Situ Real-Time X-ray Scattering. *J. Phys. Chem. Lett.* **2018**, *9*, 6750−6754.